Journal of Catalysis 433 (2024) 115456

Contents lists available at ScienceDirect

Journal of Catalysis

journal homepage: www.elsevier.com/locate/jcat

Research article

Kinetic implications of (hierarchical) zeolite fouling during liquid-phase aromatics upgrading

Hayat I. Adawi, Michele L. Sarazen *

Department of Chemical and Biological Engineering, Princeton University, NJ 08544, USA

ARTICLE INFO

Keywords:
Deactivation
Kinetics
Hierarchical zeolites
Coking

ABSTRACT

The kinetics of fouling in large pore zeolites (BEA, MOR), including those with hierarchical pore systems, were probed during the Brønsted acid catalyzed reaction of benzyl alcohol (BA) with 1,3,5-trimethylbenzene (TMB) by varying reactant driving force (i.e., $[TMB]_0/[BA]_0$; 11–119). In BEA, initial deactivation rate constants ($k_{D,0}$) decreased exponentially with $[TMB]_0/[BA]_0$, highlighting the significance of oxygenates as deactivation precursors. Further, seeding pores with oxygenates completely suppressed measured rates in parent MOR and BEA, while seeding with TMB had no effect. Comparisons of mass accumulations of different organics (low molecular weight reaction species and coke) as functions of $\ln([TMB]_0/[BA]_0)$ revealed that coke (derived from oxygenate-seeded polyalkylation of TMB) disproportionately controlled deactivation rates by damping apparent (diffusion-controlled) and intrinsic (diffusion-corrected) rate constants through proton losses and/or altered molecule confinement within shrinking pores. These kinetic consequences were delayed upon introduction of mesopores, demonstrating how zeolite porosity impacts coke proliferation and behavior in liquid-phase reactions.

1. Introduction

Growing demand for renewable fuels has motivated application of industrially ubiquitous zeolite catalysts to conversions of biomass-derived platform molecules or waste-plastics that could displace conventional petroleum feedstocks. The Brønsted acidic protons located at crystallite surfaces or confined within micropores in zeolites can impose steric selectivity on reactant ingress, transition state formation, and/or product egress [1–6]. Biomass upgrading, in particular, often involves condensed-phase systems of bulky (poly)substituted aromatics, leaving zeolites often to encounter severe or prohibitive intracrystalline diffusion barriers. The subsequently increased intracrystalline residence times potentially increase rates of undesired cascade coking reactions, which form graphitic deposits that rapidly deactivate zeolites through irreversible pore occlusion and/or proton blockage [7–11]. One method to overcome diffusion and deactivation limitations has been through the development of hierarchical zeolites, which contain auxiliary mesopores (with pore limiting diameters (PLDs) = 2–50 nm) that reportedly redistribute coke deposition [12–14], extend catalytic lifetimes [12,13,15–18], and increase selectivities to desired bulky products for a variety of reactions [9,19–21].

We previously demonstrated that bulk mass accumulations of foulants on spent (hierarchical) zeolites strongly correlated with pore surface areas and volumes during the probe liquid-phase reaction (Fig. 1) of benzyl alcohol (BA) with 1,3,5-trimethylbenzene (TMB) or itself to respectively yield 1,3,5-trimethyl-2-benzylbenzene (TM2B) or dibenzyl ether (DBE) [17,22]. Foulants included low molecular weight organics ("low organics") and graphitic coke, comprised respectively of known reaction molecules and the products of their undesired secondary transformations (including polyalkylations and hydride shifts). Low organics completely saturated (hierarchical) zeolite pores without bias toward mesopores or micropores, but coke preferentially deposited at microporous constrictions that hindered egress of bulky (poly)aromatic coking products. The effects of bulk porosity on foulant accumulations yielded broadly generalizable deactivation principles for hierarchical zeolites having wide physicochemical diversity conferred by different (post)synthetic methods and parent starting materials, yielding morphological (based on parent architecture or crystal size) and chemical (based on proton density or silanol defect density) variations. Notably, the accumulated masses of low organics and coke on spent (hierarchical) zeolites corresponded to a wide range of X_{BA} after identical (120 min) reaction times. In this current work, we ascertained the interdependence between reaction and deactivation kinetics responsible for that observation.

* Corresponding author.
E-mail address: msarazen@princeton.edu (M.L. Sarazen).

https://doi.org/10.1016/j.jcat.2024.115456
Received 15 December 2023; Received in revised form 11 February 2024; Accepted 20 March 2024
Available online 22 March 2024

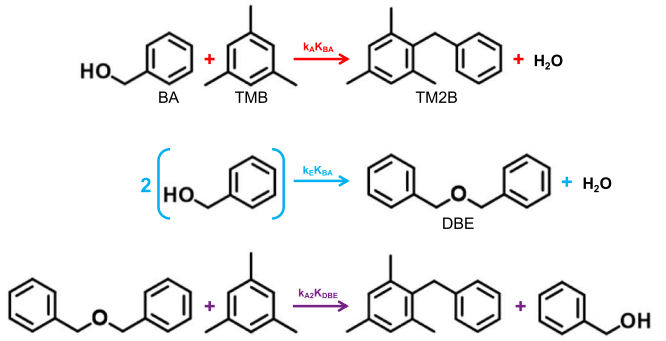

Fig. 1. TMB alkylation (red), BA self-etherification (blue), and secondary TM2B formation from DBE and TMB (violet). (For interpretation of the references to colour in this figure legend, the reader is referred to the web version of this article.)

Typically, mathematical treatments of deactivation rely on separable kinetics to easily decouple reaction rate laws from decay laws. These include decay laws that simply represent depressions of catalyst activity (a(t)) due to temporal losses in active sites [23]:

$$a(t) = \frac{-r_{A,\,decayed}(t)}{-r_{A,\,fresh}(t)} \quad (1)$$

Here, r_A represents the consumption rate of reactant A. Specific functional forms of decay depend on the mechanism of deactivation. From Eq. (1), the overall catalyst deactivation rate (r_D) follows [23]:

$$r_D = -\frac{d\,a(t)}{dt} = k_D\,g(a(t))\,f([A],\cdots,[P]) \quad (2)$$

Here, k_D is the deactivation rate constant, $g(a(t))$ represents a function of a(t), and $f([A],\ldots,[P])$ represents a function of concentrations of any reactants (i.e., A), products (i.e., P), and/or other expected precursors of deactivating species. The simplest (first-order) deactivation model with $g(a) = a$ and $f = 1$ yields an exponential integrated decay law function:

$$a(t) = e^{-k_D t} \quad (3)$$

Mathematically, a constant f means that the catalyst deactivation rate is independent of changes in any species concentrations. Practically, f is approximately constant when concentrations of deactivation species (or their precursors) greatly exceed that of a limiting reactant, as is the case when complexation of excess solvent molecules contribute to zeolite deactivation through irreversible pore occlusion.

Previous kinetic treatments of deactivation focused exclusively on microporous zeolites, particularly during coking of MFI, BEA, MOR, or USY [24–30]. Functions for a(t) were empirically determined for coking, which involves complex reaction networks that propagate polyaromatics growth until halted by steric limitations within confining (microporous) voids, resulting in deposition of coke oligomers at pore constrictions [23,27,31–33]. For catalytic cracking of 2,2,4-trimethylpentane on USY, a first-order decay law was used to model alkylation of gas-phase alkenes with carbenium ion adsorbates *via* an Eley-Rideal coke initiation mechanism [26]. On the other hand, coking of BEA during palm-oil cracking was better described by second-order decay ($g(a) = a^2$) that yielded a hyperbolic integrated function for catalyst activity [28]:

$$a(t) = \frac{1}{1 + k_D t} \quad (4)$$

The second-order dependence of the deactivation rate on catalyst activity for this latter liquid-phase system may have reflected greater concentrations of deactivation contributors in condensed-phased systems than in gas-phase systems. For our alkylation-etherification network (Fig. 1), no specific deactivation mechanism (f) has been reported. In its absence, we previously found that a first-order decay law with a constant $f = 1$ best fit experimental reaction data for 120 min of reaction on a diverse range of (hierarchical) zeolite architectures and crystal sizes [17]. This was true despite the fact that the assumption of constant f should only be valid when concentrations of deactivation species (and/or their precursors) were constant values and could be lumped into the k_D parameter (most likely at initial reaction times). Therefore, increasing concentrations of deactivation species during reaction rendered the lumped k_D a function of X_{BA} and were thus partially liable for residual errors that increased at long reaction times but seemingly averaged out with other phenomena [17]. For more rigorous assessment of deactivation timescales, even at early reaction times, this current work fitted experimental concentration data to a second-order model and used early time data ($t \leq 2$ min) when initial deactivation rate constants ($k_{D,0}$) could be accurately extracted for rigorous decoupling of reaction and deactivation rates. Values for $k_{D,0}$ were studied as indirect functions of foulant accumulation masses altering $[TMB]_0/[BA]_0$, which impacted \formation rates of deactivation precursors. Use of one zeolite sample (BEA) enabled control of intrinsic kinetics, which were characterized with diffusion-corrected alkylation and diffusion-corrected etherification rate constants. The long-term ($0 \ll X_{BA} \leq 1$) impacts of low organics and coke accumulations on intrinsic rates were then contrasted between parent (BEA, MOR) and hierarchical (MOR-h) zeolites, to probe the effect of mesopores on the timescale of kinetically relevant deactivation. We broadly define *kinetically relevant deactivation* in Brønsted acidic (hierarchical) zeolites as irreversible reductions in apparent and/or intrinsic reaction rates. These reductions are functions of time-on-stream or clock time, due to proton poisoning or pore occlusion. Reaction selectivities may or may not be impacted in consequence, as selectivities of parallel or sequential rates depend on the relative impacts of pore constriction on diffusion and/or confinement of pathway moieties [34,35]. This work fundamentally contextualizes the vulnerabilities of zeolite catalysts in reaction systems where deactivating species readily form and propagate, in order to advance design of next generation catalysts.

Table 1
Samples of synthesized and commercial zeolites. Values in parenthesis represent one standard deviation.

Catalyst	Si/Al	$[H^+]$ [a]	$d_{crystal}$ [b]	Surface Area [c]		
				BETSI	micro	meso
BEA	12.5	0.72	0.19 (0.11)	670 (20)	280 (30)	290 (80)
MOR	10	1.3	0.17 (0.09)	630 (20)	460 (30)	110 (80)
MOR-h	17	0.79	0.17 (0.04)	550 (20)	93 (30)	310 (80)

[a] (mmol/g);
[b] (μm);
[c] (m^2/g).

2. Materials and methods

2.1. Post-synthetic treatments of commercial zeolites

Commercial NH_4-BEA (Zeolyst CP814E, Si/Al = 12.5) and NH_4-MOR (CBV 21A, Si/Al = 10, Zeolyst) were NH_4^+-exchanged, washed with deionized H_2O, and dried to yield re-exchanged NH_4-BEA and NH_4-MOR following previous methods [17]. The re-exchanged catalysts were then calcined for 8 h at 823 K under 150 standard cubic centimeters per minute (sccm) air (zero grade; Airgas) to yield their proton analogs denoted without a hyphenated prefix (MOR, BEA).

MOR-h was prepared by post-synthetic leaching of MOR following previous methods [17]. Briefly, Na-MOR-h was first prepared by dealumination of MOR in 2 M HNO_3 for 4 h at 373 K, followed by desilication in 0.2 M NaOH (30.3 mL/g MOR) at 338 K for 30 min [36–38]. Na-MOR-h was then thrice NH_4^+-exchanged, washed, and dried to yield NH_4-

MOR-h.

2.2. Characterizations of (hierarchical) zeolite samples

Table 1 summarizes the textural and chemical properties of BEA, MOR, and MOR-h. Crystal sizes were deduced from transmission electron microscopy (TEM; Talos F200X Scanning/Transmission Electron Microscope) at 200 kV of zeolites dispersed on Formvar carbon film 400 mesh Cu grids after sonication (~15 min) in acetone. Si/Al were measured by energy-dispersive X-ray spectroscopy (EDXS; XL30 FEG-SEM) at 5 kV of zeolites dusted onto carbon tape mounted on metal sample studs.

N_2 physisorption isotherms (77 K) were collected using a Micromeritics 3Flex for samples degassed overnight (125 torr at 423 K) on a Schlenk line. The ambient and analysis free space volumes were respectively set to 16 cm^3 and 45 cm^3. Brunauer-Emmett-Teller surface areas (S_{BET}) were calculated using the BET Surface Identification (BETSI) software with the Rouquerol criteria listed for each catalyst in Table A1 [39]. Brunauer-Joyner-Halenda (BJH) mesopore surface areas (S_{meso}) were calculated from the adsorption data of the N_2 physisorption isotherms using a Harkins and Jura thickness curve with Faas correction for pore diameters from 2 to 50 nm [40,41]. Micropore surface areas (S_{micro}) were calculated using the t-plot method with a Harkins and Jura thickness curve. Further details of physisorption measurements and methods were undertaken identically to previously reported protocol [22].

Proton densities were measured from temperature-programmed desorption of ammonia (NH_3-TPD; Micromeritics Autochem II). A given zeolite sample (20–50 mg) was loaded into a U-tube reactor packed with quartz wool (4 μm, Thermo Fisher Scientific) and pretreated *in-situ* by drying at 673 K for 240 min under He (ultra-high purity; Airgas) at 30 sccm, followed by cooling to 373 K for saturation with NH_3 (10 % in He; Airgas) at 30 sccm for 120 min. The sample was then flushed with He (30 sccm) for 60 min at 373 K to remove physisorbed NH_3. All outflow gases for these pretreatments bypassed the thermal conductivity detector (TCD) and were directly vented to an elephant trunk. Pretreated samples were heated from 373 to 973 K in He (30 sccm), with the outflow routed to the TCD calibrated for the concentration of NH_3. Proton densities (mmol/g catalyst) were calculated from integrated NH_3 signals centered at 623–673 K.

2.3. Alkylation of 1,3,5-trimethylbenzene (TMB) with benzyl alcohol (BA)

In a typical batch kinetics experiment adapted from previous methods [17], the freshly calcined proton-form of the catalyst was immediately loaded into a two-neck, round-bottom flask and charged with TMB (9.2–9.75 mL, 99 %, Acros Organics). The flask reactor was fitted with a magnetic stirrer, connected through one neck to a reflux condenser, capped at the second neck with a rubber septum, and submerged in a temperature-controlled oil bath (363 K) for 90 min. The bath was then heated to reaction temperature (393 K), at which point BA (0.06–0.61 mL, 99.97 %, Chem Impex International) was injected to initiate reaction (t = 0 min). Aliquots (t = 0, 2, 10, 20, 30, 45, 80, 120 min) were extracted through the rubber septum using a syringe fitted with a 16 G needle (to prevent clogging), filtered through a cotton-plugged Pasteur pipette into a glass vial, and immediately quenched through refrigeration.

Aliquots (20 μL) were sampled and diluted in $CDCl_3$ (600 μL, 99.8 % atom D, Sigma-Aldrich) for ^{1}H NMR (500 MHz) analysis utilizing the following chemical shifts BA: δ 4.63 (s, 2H). DBE: δ 4.55 (s, 4H). TM2B: δ 4.30–2.50 (m, 2H). The spent catalysts were separated from the remaining reaction broths *via* centrifugation The collected, spent catalysts were air-dried in a fume hood for at least 72 h before thermogravimetric analysis following Section 2.6.

Fractional BA conversions (X_{BA}) at each time point were calculated relative to the integrated ^{1}H NMR signal for BA at t = 0 min. The fractional selectivity of BA to form TM2B over DBE (S_{TM2B}) at each time point was also calculated from the relative changes in integrated ^{1}H NMR signals for BA and TM2B:

$$S_{TM2B,t} = \frac{A_{TM2B,0} - A_{TM2B,t}}{A_{BA,0} - A_{BA,t}} \quad (5)$$

The calculation in Eq. (5) assumed that TM2B and DBE were the sole reaction products in the reaction broth. This assumption was verified by homo-decoupled ^{1}H NMR [22], and it also enabled calculation of mass balances on a BA basis for all spent catalysts from ^{1}H NMR signal areas for BA, TM2B, and DBE:

$$MB = \left(\frac{A_{BA,t} + A_{TM2B,t} + A_{DBE,t}}{A_{BA,0}}\right) \quad (6)$$

Early concentration data (t ≤ 2 min) were nonlinearly regressed to a differential reaction network model with a second-order deactivation term:

$$\frac{-r_{BA}}{[H^+]} = \frac{k_A K_{BA}[TMB][BA]^\beta + k_E K_{BA}[BA]^\beta - k_{A2} K_{DBE}[TMB][DBE]^\beta}{1 + k_D t} \quad (7)$$

$$\frac{r_{TM2B}}{[H^+]} = \frac{k_A K_{BA}[TMB][BA]^\beta + k_{A2} K_{DBE}[TMB][DBE]^\beta}{1 + k_D t} \quad (8)$$

$$\frac{r_{DBE}}{[H^+]} = \frac{k_E K_{BA}[BA]^\beta - k_{A2} K_{DBE}[TMB][DBE]^\beta}{1 + k_D t} \quad (9)$$

Microporous zeolites were modeled with reduced reaction orders (β) equivalent to $\beta = (n + 1)/2$, where $\beta = 3/2$ for second-order (n = 2) BA self-etherification and $\beta = 1$ for pseudo first-order (n = 1) alkylation with respect to [BA] [42]. Reduced orders were due to assumed operation in the diffusion limit and were consistent with published accounts of severe diffusion constraints for this reaction system in microporous BEA, MOR, and MFI [21,43–45], as well as DFT-calculated vdW diameters (d_{vdW}) of TMB, TM2B, and DBE relative to pore-limiting diameters of zeolite micropores [17]. Similarly, $\beta = 1$ for pseudo first-order (n = 1) secondary consumption of DBE.

2.4. Dibenzyl ether (DBE) consumption

Ammonium-exchanged catalyst (0.1 g) was calcined and loaded with TMB (9.8 mL) into a two-neck, round-bottom flask following Section 2.3. After isothermal TMB equilibration (363 K) for 90 min, the broth was heated to reaction temperature (393 K), at which point DBE (0.04 mL, 98 %, Sigma-Aldrich) was injected to initiate reaction (t = 0 min). Aliquots (t = 0, 2, 10, 20, 30, 45 min) were extracted and analyzed with ^{1}H NMR following Section 2.3, absent BA analysis.

2.5. Neat BA self-etherification

Ammonium-exchanged catalyst (0.1 g) was calcined to its proton form. Separately, BA (9.6 mL) was charged into a two-neck, round-bottom flask fitted with a magnetic stirrer, connected through one neck to a reflux condenser, and capped at the second neck with a rubber septum. The reactor was submerged in a temperature-controlled oil bath (298 K), which was then heated to reaction temperature (393 K). At temperature, the reflux condenser was briefly disconnected to add the catalyst to initiate reaction (t = 0 min). Aliquots (t = 0, 2, 10, 20 min) were extracted and analyzed for X_{BA} following Section 2.3.

2.6. Thermogravimetric analysis (TGA)

TGA was performed using a Perkin Elmer TGA 8000. Briefly, spent catalysts (1–10 mg) were loaded into ceramic crucibles. The loaded

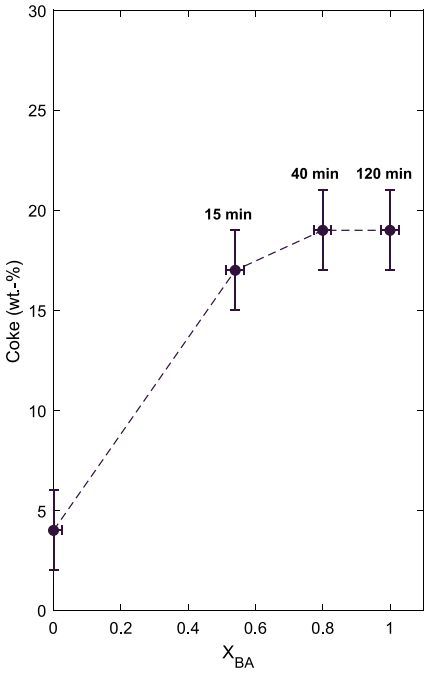

Fig. 2. X_{BA} and coke (wt.-%) at t = 15, 40, and 120 min ($[TMB]_0/[BA]_0 = 33$, 393 K, 0.1 g BEA, 9.8 mL total batch volume).

samples were first dried isothermally at 353 K for 3 h under Ar (ultra-high purity; Airgas). Samples were then heated from 353 to 1173 K (10 K/min) under 90 sccm air (zero grade; Airgas). Weight percent accumulations of total organics (353–1173 K), low organics (353–673 K), and coke (673–1173 K) were calculated relative to freshly calcined, dry catalyst masses at 1173 K following previous methods [22]. Error bars were calculated from triplicate measurements.

3. Results and discussion

3.1. Temporal development of coke during a single catalytic cycle

Coke accumulations measured from post-reaction TGA were compared to X_{BA} for BEA at a fixed reactant concentration ($[TMB]_0/[BA]_0 = 33$; Fig. 2) to probe how the temporal progression of deactivation impacted catalyst activity. Coke accumulations increased with X_{BA} until t = 40 min, after which X_{BA} continued increasing without additional measurable coke formation. This plateau could potentially be consistent with complete occlusion of internal catalyst pores, relegating catalytic turnovers to protons at the crystallite surface that lacked confining environments amenable to coke (precursor) deposition. The specific locations and impacts of coke deposition in BEA are dictated by the pore architecture and channel dimensionality of that framework. Here, the persistence of catalytic activity in BEA after maximum coke saturation (as inferred from the plateau of coke accumulation) suggests the continued accessibility of protons on and/or from the external crystal surface to respectively facilitate surface turnovers and/or reactant ingress. This implied that coke did not significantly accumulate on external BEA surfaces. However, foulant accumulation at external zeolite surfaces was reported by other groups [8,46–48].We also previously inferred that graphitic coke preferentially accumulated at the external surface of an MFI sample synthesized with an Al-rich crystal shell. This was observed first from higher measured nominal [Al] in the crystal shell (where Si/Al = 11) than the crystal core (where Si/Al = 57) using energy-dispersive X-ray spectroscopy, which suggested a higher proton density in the shell that could catalyze coking. This zoned MFI accumulated more coke within 120 min during TMB alkylation than an MFI sample with uniformly distributed Al. Moreover, the complete suppression of TMB alkylation rates upon selective titration of surface protons of the zoned MFI with an alkylpyridine poison (1,3,5-trimethylpyridine) similar in size to TMB indicated that any formation of coke molecules inside the 10-MR MFI pores was derived from DBE, because TM2B was not formed internally [17,22]. Clearly, the effects of porosity on foulant accumulation must be carefully considered in comparisons of deactivation across different zeolite architectures. For this reason, our work here specifically examined deactivation kinetics within the context of one (BEA) zeolite pore architecture.

3.2. Isolating the effects of reactant concentrations on zeolite fouling

To probe the impacts of deactivation on X_{BA}, deactivation rates were independently varied by changing the initial BA concentration ($[TMB]_0/[BA]_0 = 11$–119) for a reaction series on a single batch of BEA (Section 2.3). Because BA is involved in both TM2B and DBE formation (and reacts in second order for DBE formation), higher $[BA]_0$ would likely increase initial reaction rates and therefore increase deactivation rates due to faster formation of reaction products that can form carbonaceous deposits. Observed damping of temporal X_{BA} profiles at sub-unity values

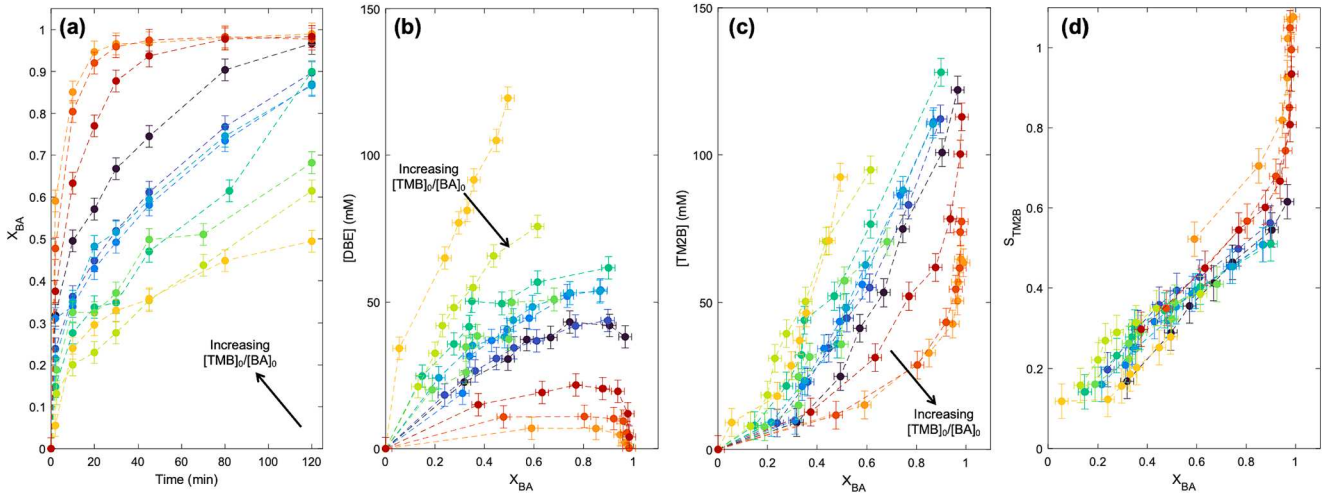

Fig. 3. (a) Temporal X_{BA} for alkylation-etherification with $[TMB]_0/[BA]_0 = 11$ (●), 16 (●), 22 (●), 24 (●), 25 (●), 27 (●), 31 (●), 33 (●), 60 (●), 90 (●), 119 (●). Corresponding (b) DBE and (c) TM2B concentrations (mM) and (d) S_{TM2B} as functions of X_{BA} (393 K, 0.1 g BEA, 9.8 mL total batch volume).

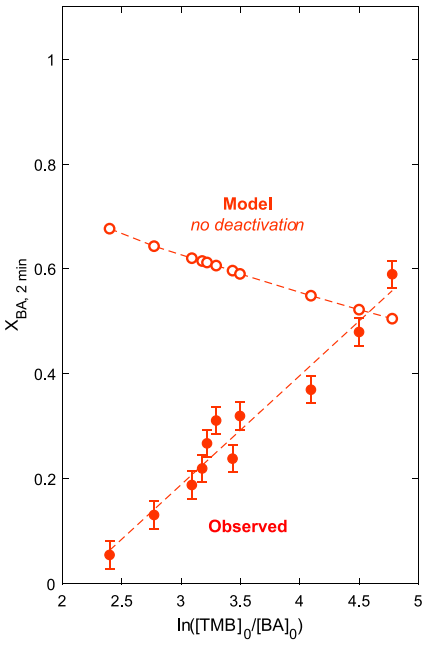

Fig. 4. $X_{BA,\ 2\ min}$ as a function of $\ln([TMB]_0/[BA]_0)$, determined both experimentally (●) and modeled without deactivation (○) using fitted rate constants (393 K, 0.1 g BEA, $[TMB]_0/[BA]_0$ = 11–119, 9.8 mL total batch volume). Dashed lines are fitted linear regression models.

with decreasing $[TMB]_0/[BA]_0$ (Fig. 3a) was consistent with higher coking rates at greater $|-r_{BA}|$. If deactivation had otherwise not impacted X_{BA}, then X_{BA} would have decreased with increasing $[TMB]_0/[BA]_0$ at equivalent times because $|-r_{BA}|$ scales with [BA], which controls the forward driving force of both reactions (Fig. 4).

The plateau in experimental temporal X_{BA} was also more significant than what would be expected from reactant consumption alone, as previously discussed for this same alkylation system on BEA, MOR, and MFI [17]. DBE and TM2B yields (Fig. 3b-c) at equivalent X_{BA} increased with $[BA]_0$ because of the greater reaction driving force (similarly shown as temporal yields Fig. S2). This overall driving force deconvolutes into separate formation rates for DBE and TM2B, for which the relative selectivity (S_{TM2B}; Eq. (5) changed identically with X_{BA} for all $[TMB]_0/[BA]_0$ = 11–119 (Fig. 3d). Therefore, greater deactivation at lower $[TMB]_0/[BA]_0$ did not observably impact S_{TM2B}, which consistently approached $S_{TM2B} = 1$ due to the secondary consumption of DBE to form TM2B (reaction (3), Fig. 1). Further, selectivity to DBE (where $S_{DBE} = 1\text{-}S_{TM2B}$) did not significantly increase with $[BA]_0$ at equivalent X_{BA} because even the lowest value was still excess TMB. The varying onset times of net DBE consumption occurred at similar X_{BA} rather than at similar times, so analysis of temporal [DBE] and [TM2B] was less insightful.

3.3. Extracting the relative significance of different foulant types on reaction kinetics

Given that the above data suggested that $[TMB]_0/[BA]_0$ represented the inverse reaction driving force, its influence on turnover rates was most simply deduced from the slope of a linear correlation between it and X_{BA} at equivalent clock times on BEA. Accordingly, the natural logarithm of the inverse driving force ($\ln([TMB]_0/[BA]_0)$) exhibited strong linear correlations with X_{BA} and at both early clock times (t = 2 min; Pearson's r = 0.96) and late (t = 120 min; r = 0.83) clock times (Fig. 5a). This linear correlation held until $[TMB]_0/[BA]_0$ = 33 for $X_{BA,120\ min}$, and then plateaued (as $X_{BA,120\ min} = 1$ for $[TMB]_0/[BA]_0 \geq 33$). Accumulations of low organics and coke (deduced from Section 2.6) were also linearly regressed as functions of $\ln([TMB]_0/[BA]_0)$ at 2 min and 120 min (Fig. 5b-c). Differential TGA mass profiles for calcined BEA samples for each $[TMB]_0/[BA]_0$ are included in the Supplementary Information (Fig. S3):

$$\text{accumulation}_{i,j} = \alpha_{i,j}\ln([TMB]_0/[BA]_0) + \gamma_{i,j} \quad (10)$$

where i represents either low organics or coke and j indicates the reaction duration (2 or 120 min). $|\alpha_{i,j}|$ is a response factor that quantifies the relative unit increase of coke or low organics accumulation for each unit increase in $\ln([TMB]_0/[BA]_0)$. If $|\alpha_{i,j}| > 0$, then coke (or low organics) accumulation was compounded for unit increases in $[BA]_0$. We hypothesized that if coking was driven by cascade polyalkylation reactions primarily propagated by TMB solvent after initiation by a BA-derived oxygenate molecule, then $|\alpha_{coke,j}| \gg 0$ due to disproportionately

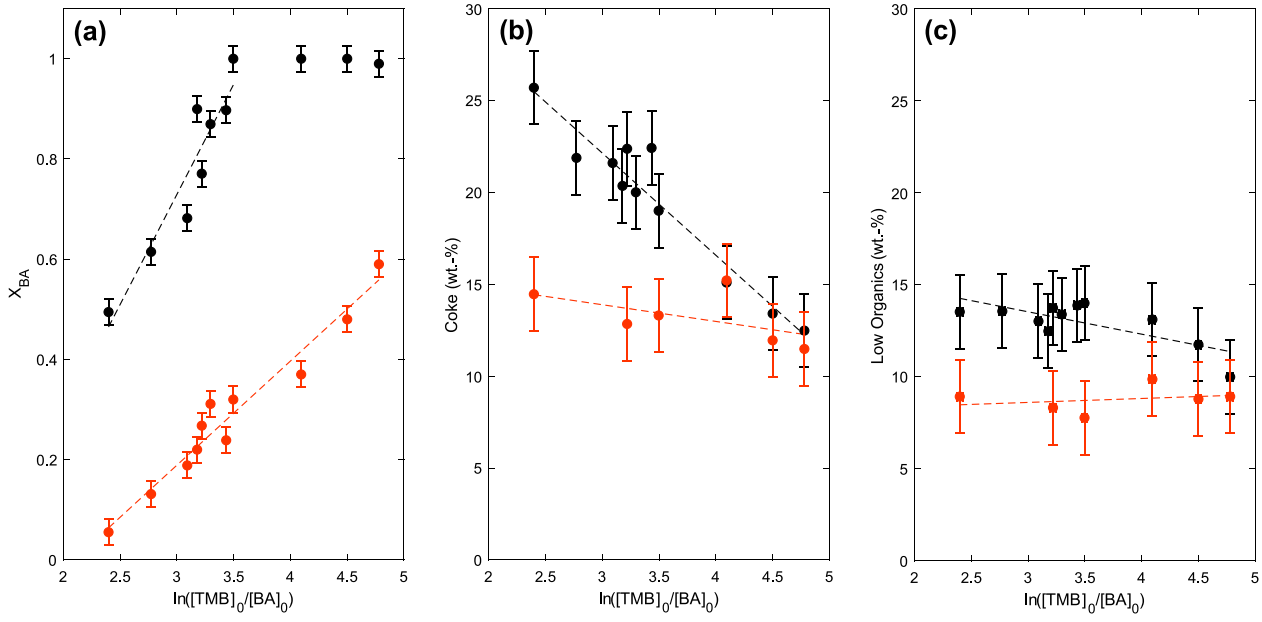

Fig. 5. (a) X_{BA}, (b) coke accumulations (wt.-%), and (c) low organics accumulations (wt.-%) as functions of $\ln([TMB]_0/[BA]_0)$ after 2 min (●) and 120 min (●) of reaction (393 K, 0.1 g BEA, $[TMB]_0/[BA]_0$ = 11–119, 9.8 mL volume). Dashed lines are fitted linear regression models.

Table 2
Slopes (α), intercepts (γ) and Pearson's r for correlations between $\ln([TMB]_0/[BA]_0)$ and accumulations (wt.-%) of coke or low organics for $[TMB]_0/[BA]_0$ = 11–119 after 2 min or 120 min. Values in parentheses represent 95 % confidence intervals.

Foulant *i*	Time (min) *j*	α (wt.-%)	γ (wt.-%)	Pearson's *r*
Coke	2	−0.91 (1.86)	16 (7)	−0.56
	120	−5.6 (1.2)	39 (4)	−0.96
Low Organics	2	0.21 (0.84)	8.0 (4.1)	0.27
	120	−1.2 (1.1)	17 (3)	−0.74

increasing rates of coking relative to BA consumption. γ_{ij} quantified the extrapolated accumulation of low organics or coke when initial reactant concentrations were equivalent ($[TMB]_0 = [BA]_0$ and $\ln([TMB]_0/[BA]_0 = 0$) and represented the stoichiometric limits for TM2B and DBE production. Indeed, coke accumulation decreased with increasing $[TMB]_0/[BA]_0$ at both $X_{BA,2\ min}$ and $X_{BA,120\ min}$, but the more pronounced effect at 120 min ($\alpha_{coke,120}$ = -5.6 ± 1.2 wt-%) than at 2 min ($\alpha_{coke,2}$ = -0.91 ± 1.86 wt-%) was consistent with expected higher deactivation rates at 120 min due to higher concentrations of DBE and TM2B as coke precursors (Table 2). We note that the high error for $\alpha_{coke,2}$ (±1.86 wt-%) resulted from the outlier at $\ln([TMB]_0/[BA]_0) \approx 4$ and does not imply inaccuracy of linear regression; discounting the outlier gave ($\alpha_{coke,2}$ = -1.2 ± 0.56 wt-%). In contrast, changes in $[TMB]_0/[BA]_0$ affected accumulations of low organics more modestly at 2 min ($\alpha_{low\ organics,2}$ = 0.21 ± 0.84 wt-%) and 120 min ($\alpha_{low\ organics,120}$ = -1.2 ± 1.1 wt-%), implying greater kinetic relevance of coking than of saturation with known reaction moieties, with increasing relevance at longer clock times as $\alpha_{coke,j}$ increased significantly. In fact, the statistical independence $\alpha_{low\ organics,j}$ on clock time indicates no impact of low organics accumulation on reaction kinetics. Further, Pearson's r analysis of $\ln([TMB]_0/[BA]_0)$ correlations with low organics and coke accumulations (Table 2) confirmed that the weakest correlation was with low organics at 2 min (r = 0.27). For $\gamma_{i,j}$ values at $[TMB]_0 = [BA]_0$ mass accumulations were at the limit of stoichiometric ratios for TMB alkylation and BA self-etherification. This threshold corresponded to the bound at which S_{TM2B} profiles would deviate from Figure 3d.

Similar correlative analyses were undertaken for accumulations of coke and low organics as functions of $X_{BA,\ 2\ min}$ and $X_{BA,\ 120\ min}$ (Fig. S4). Importantly, these correlations were less meaningful because they lacked direct causation, as values of $X_{BA,\ 2\ min}$ and $X_{BA,\ 120\ min}$ were manifestations of changes in the inverse reaction driving force ($[TMB]_0/[BA]_0$). Consequently, $X_{BA,\ 2\ min}$ and $X_{BA,\ 120\ min}$ bore the same correlative trends with foulant accumulations as $\ln([TMB]_0/[BA]_0)$: coke accumulation strongly correlated with $X_{BA,\ 2\ min}$ (r = -0.61; Table S1) and $X_{BA,\ 120\ min}$ (r = -0.82), while low organics accumulation correlated weakly with $X_{BA,\ 2\ min}$ (r = 0.12) and with $X_{BA,\ 120\ min}$ (r = 0.08). Therefore, all subsequent kinetics analyses were based on direct relationships with $[TMB]_0/[BA]_0$. However, Figure S4 does show how low organics accumulation remain stagnant throughout 120 min across $[TMB]_0/[BA]_0$ while coke accumulation decreases significantly with greater $[TMB]_0/[BA]_0$ at both 2 min and 120 min.

Notably, mass balances on a BA basis (Eq. (6)) were approximately closed (99 ± 1.2 %, where 1.2 % represents the magnitude of a 95 % confidence interval range; Fig. 6) for all X_{BA} and $[TMB]_0/[BA]_0$. As these mass balances were calculated from species concentrations outside of the catalyst (from the filtered reaction liquid), any mass balances significantly below 100 % would suggest that reaction products were significantly and irreversibly accumulating within BEA pores. This result refutes the presumed hypothesis that mass balances would decrease with increasing foulant accumulation. Likewise, we initially hypothesized that mass balances would decrease with $[TMB]_0/[BA]_0$ at equivalent X_{BA}, due to concomitant increases in coke precursor formation rates. Therefore, the closed mass balances instead indicated that DBE and TM2B were not significantly consumed during deactivation. It could be

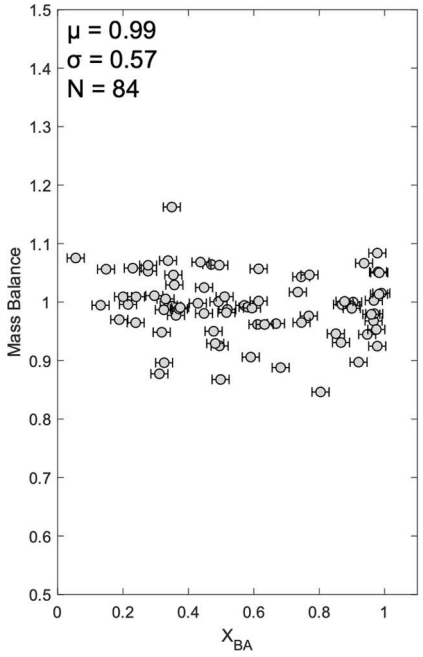

Fig. 6. All mass balances (393 K, 0.1 g BEA, 9.8 mL total batch volume) as a function of X_{BA}, with mean (μ) and standard deviation (σ) of N = 84 data points. Error bars represent 95 % confidence intervals.

that immeasurably small quantities of DBE and TM2B seeded coke formation, and that TMB solvent was the primary coke feedstock. This possibility was supported by disproportionately high increase in coke accumulation with unit increases in $[BA]_0$ ($\alpha_{coke,j}$; Table 2) and is further supported in later in Section 3.4. Here, consumption of TMB for coking was undetectable because it was in high molar excess of all other molecules.

Initial deactivation rate constants ($k_{D,0}$) were extracted by fitting early concentration data to Eqs. (7)–(9) (where $k_D = k_{D,0}$) to probe the kinetics of coke accumulation. Unlike the first-order decay law that was previously used to described activity at conversions up to $X_{BA} = 1$ [17], the second-order decay law here better described low X_{BA} data (Fig. S1). While some damping models reportedly fit certain deactivation mechanisms (pore occlusion or sintering) better than others, they are ultimately empirical [23].Values for $k_{D,0}$ scaled logarithmically (natural) with $[TMB]_0/[BA]_0$ (Fig. 7a) with two deactivation regimes that converged near $[TMB]_0/[BA]_0 = 33$ (Fig. 7b). Values of $k_{D,0}$ were linearly regressed for Regime 1 ($[TMB]_0/[BA]_0 < 33$) and Regime 2 ($[TMB]_0/[BA]_0 > 33$) as functions of $[TMB]_0/[BA]_0$ (Table 3):

$$\ln(k_{D,0}) = \delta_i[TMB]_0/[BA]_0 + \lambda_i \quad (11)$$

where i represents the regime and δ_i and λ_i both have units of $\ln(min^{-1})$. $|\delta_i|$ quantified the marginal increase in deactivation with increasing $[BA]_0$. λ_i represented the extrapolated deactivation response to neat BA charge ($[TMB]_0 = 0$). The ratio of δ_1 ($|\delta_1| = 0.12 \pm 0.04$) to δ_2 ($|\delta_2| = 0.031 \pm 0.017$) of $\delta_1/\delta_2 = 3.9 \pm 0.6$ suggests that, for each unit increase in $[TMB]_0/[BA]_0$, the subsequent increase in $\ln(k_{D,0})$ within Regime 1 was approximately quadruple that of Regime 2. The validity of λ_1 as the highest possible value of $\ln(k_{D,0})$ would require that rapid coking occur under neat BA conditions, meaning that the oxygenated BA self-etherification product (DBE) had to supersede the TMB alkylation product (TM2B) as the primary coke precursor. Additionally, this meant that coking could propagate even in the absence of TMB as a polyalkylation feedstock. The validity of these scenarios was probed later in Section 3.4.

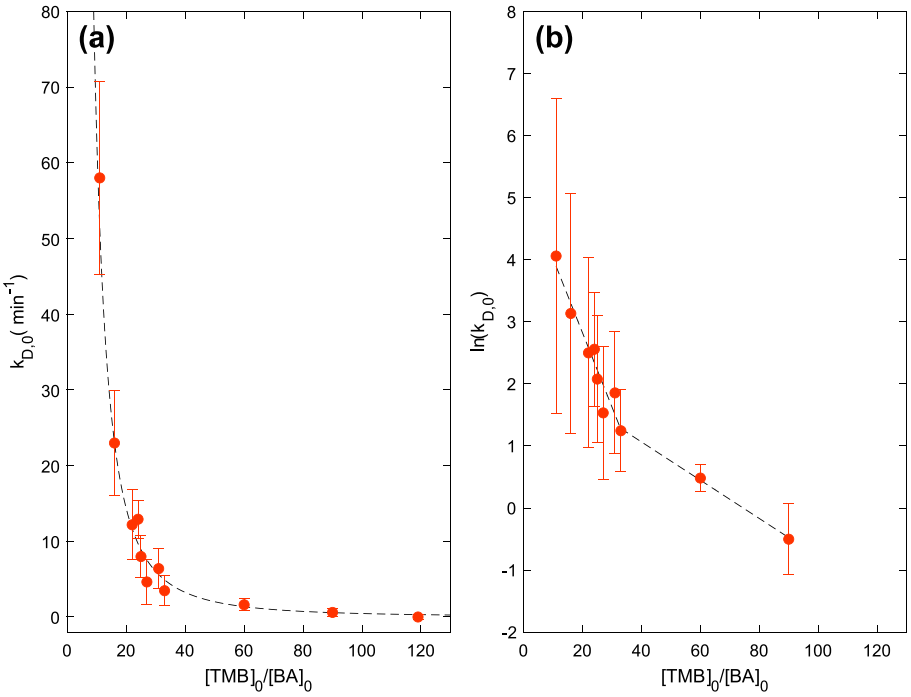

Fig. 7. Fitted $k_{D,0}$ (min^{-1}) as a (a) function of $[TMB]_0/[BA]_0$ and as a (b) semilogarithmic function of $[TMB]_0/[BA]_0$ (393 K, 0.1 g BEA, 9.8 mL volume).

Table 3
Fitted slopes (δ) and y-intercepts (λ) for $\ln(k_{D,0})$ dependence on $[TMB]_0/[BA]_0$ extracted for ($t \leq 2$ min). Values in parenthesis represent 95 % confidence intervals.

$[TMB]_0/[BA]_0$	Regime (*i*)	δ_i	λ_i
< 33	1	−0.12 (0.04)	5.2 (0.9)
> 33	2	−0.031 (0.017)	2.3 (1.1)

3.4. *Delaying the kinetic response of zeolites to foulant deposition using mesopores*

Since apparent reaction rates (changed *via* $[TMB]_0/[BA]_0$) affected deactivation, the complementary impacts of varying zeolite structures on the response to identical deactivation conditions was probed using BEA, MOR, and MOR-h. MOR and MOR-h were leveraged to compare effects of auxiliary mesoporosity ($\Delta V_{meso} = +180$ % relative to parent) [22]. To reduce the number of simultaneously fitted reaction parameters compared to Eqs. (7)–(9), we exclusively probed the reaction of DBE with TMB to form TM2B (Fig. 8) by charging DBE instead of BA into the reactor at t = 0 min (Section 2.4). We note that homo-decoupled ^{1}H NMR confirmed that no other products formed. As a control, TMB was allowed to equilibrate within BEA pores (Treatment A, Table 4) before charging DBE, giving $k_{A2,A}K_{DBE}[H^+] = 0.26 \pm 0.09$ M^{-1} s^{-1}. This apparent lumped rate constant was not site-normalized, to enable comparisons with rate constants on deactivated samples with altered $[H^+]$. When TMB equilibration was followed by activated TMB adsorption (Treatment A′; Table 3), no significant decreases in k_{A2} were measured ($k_{A2,A'}/k_{A2,A} = 1.1$), indicating that protons did not catalyze coking from TMB alone. Here, *activated TMB adsorption* refers to adsorptive interactions that occur at elevated temperatures to facilitate diffusion. Here, activated TMB adsorption was probed at our standard reaction temperature (393 K) to account for baseline foulant accumulation that may have formed in the absence of BA. When control TMB equilibration was instead followed by alkylation-etherification (Treatment A″) to completion ($X_{BA} = 1.0$) before spiking additional DBE, the k_{A2} significantly reduced ($k_{A2,A''}/k_{A2,A} = 0.042$). Similar trends held for the analogous treatments for MOR-h ($k_{A2,B''}/k_{A2,B} = 0.0$) and MOR ($k_{A2,C''}/k_{A2,C} = 0.21$) whereby B (and B″) or C (and C″) respectively index the control (and alkylation-etherification) treatment for MOR-h and MOR. In all cases, the alkylation-etherification treatment damped apparent k_{A2} when additional DBE was spiked. Therefore, kinetically relevant deactivation only occurred when oxygenated products seeded coke, but the excess TMB acted as the (aromatic) carbon source, propagating coke formation at 393 K *via* polyalkylation at its aromatic ring. Aliphatic solvents, especially alkanes, would likely not propagate coking to similar extent at these conditions due to the high temperatures required for endothermic dehydrogenation that initiates the cascade of alkane conversions to alkenes and subsequent cyclization to aromatics (≥573 K) [49]. The damping of apparent k_{A2} increased with MOR > BEA > MOR-h, consistent with reduced damping for increased diffusivities due to greater prevalence of large, interconnected (meso)pores. Among MOR, BEA, and MOR-h, MOR exhibited the lowest mesopore surface $S_{meso} = 110 \pm 80$ m^2/g, and only allowed diffusion along a single axis, whereas BEA inherently has a 3D network with large voids formed at intersections of its 12-MR channels. MOR-h has a similar mesopore surface area (310 ± 80 m^2/g) to BEA (290 ± 80 m^2/g), but desilication enhances mesopore connectivity to the crystal surface. Thus, the enhanced diffusion of products reduces their contact time with internal protons that cause secondary coking turnovers.

Kinetically relevant deactivation clearly proceeded through coking, which we are proposing from the above analysis was initially seeded by oxygenated reaction products and then propagated by excess TMB. Isolation of the BA self-etherification pathway (Fig. 9) enabled exclusive probing of coke formation from DBE. When comparing temporal DBE formation in neat BA and during alkylation-etherification at our highest initial BA loading ($[TMB]_0/[BA]_0 = 11$), BEA activity plateaued at much lower X_{BA} in neat BA ($X_{BA} \ll 0.01$; Fig. 9). than in excess TMB ($X_{BA} \ll 0.6$; Fig. 2); a concomitant and more severe discoloration of BEA (from white to deep amber) within 20 min in the former due to the high concentration of oxygenates like DBE acting as primary coking seeds. Preferential coking from DBE is consistent with the stronger interactions of zeolitic protons with DBE (*via* dipole–dipole interactions with the bridging oxygen atom in DBE) than with TM(2)B (*via* π-interactions with the aromatic ring(s)). These relative interactions were previously

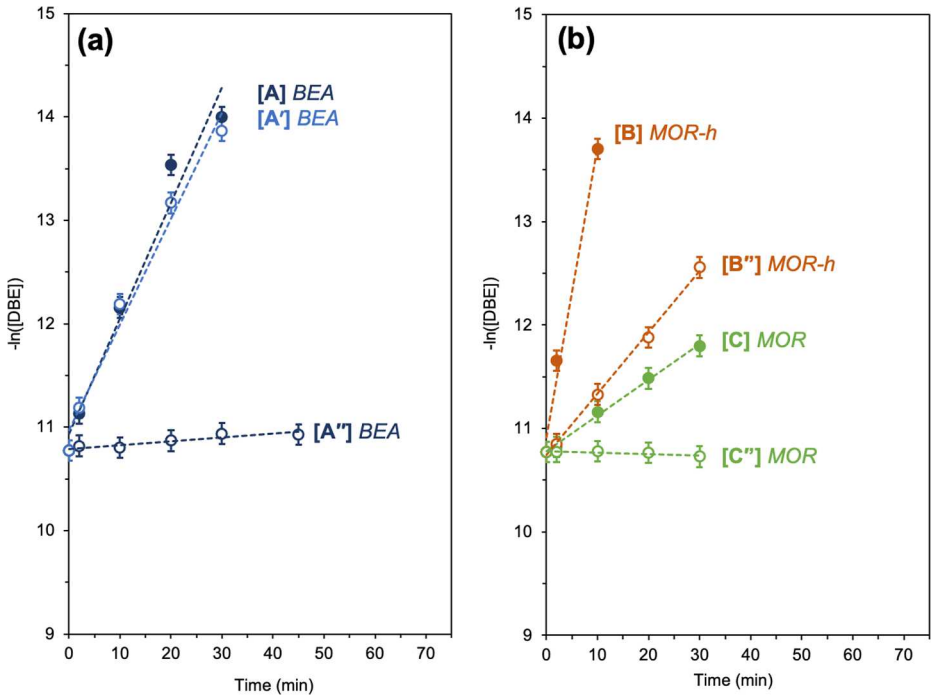

Fig. 8. (a) Fitted DBE consumption (393 K, 9.8 mL TMB, 0.04 mL DBE, 0.1 g catalyst) on BEA after 90 min TMB equilibration (363 K; A●), plus either 120 min TMB adsorption (393 K; A′○) or alkylation-etherification (393 K; A″○). (b) Fitted DBE consumption after 90 min TMB adsorption on MOR-h (B●) and MOR (C●), plus alkylation-etherification (B″○ and C″○, respectively).

Table 4
Fitted pseudo first-order DBE consumption rate constants (k_{A2}) for BEA, MOR, and MOR-h after varying catalyst pretreatments. All pretreatments done at 393 K and for 120 min. Values in parenthesis are 95 % confidence intervals.

Catalyst	Index (i)	Pretreatment	$k_{A2,i}K_{DBE}[H^+]$ [a]
BEA	**A**	control	0.26 (0.09)
	A′	**A** + TMB adsorption	0.28 (0.06)
	A′′	**A** + TMB alkylation	0.011 (0.007)
MOR-h	**B**	control	0.673 (0.930)
	B′′	**B** + TMB alkylation	0.142 (0.012)
MOR	**C**	control	0.084 (0.009)
	C′′	**C** + TMB alkylation	0.00 (0.00)

[a] (M^{-1} s^{-1}).

gleaned from energetically minimized conformations of statically adsorbed DBE and TM2B in BEA using DFT [17,22]. Here, the more energetically favorable interactions of oxygenates with zeolitic protons reflected a greater reactivity of protons toward oxygenates. Coking mediated by DBE thus encountered lower gross energy barriers than coking mediated by TMB – consistent with insignificant damping of intrinsic catalytic rates upon pretreatment in TMB solvent at elevated temperatures (Fig. 8).

The greater damping of DBE conversion rates on parent zeolites than on hierarchical zeolites following intentional deactivation (Fig. 8) suggested that kinetic manifestations of coking were mitigated by mesopores. To further explore the potential for mesopores to delay onset of kinetically relevant deactivation, coke accumulations at various X_{BA} were next compared for MOR and MOR-h. Higher X_{BA} ($X_{BA} = 1.00 \pm 0.03$; Fig. 10a) and coke accumulation (23 ± 1 wt-%; Fig. 10b) were measured on MOR-h compared to MOR ($X_{BA} = 0.49 \pm 0.03$ and 10 ± 1 wt-% coke) at equivalent clock times (120 min). This was compared to *iso*-conversion data ($X_{BA} = 0.49 \pm 0.03$) for MOR and MOR-h obtained at 120 min and 5.5 min, respectively (Fig. 10a). At equivalent X_{BA}, more

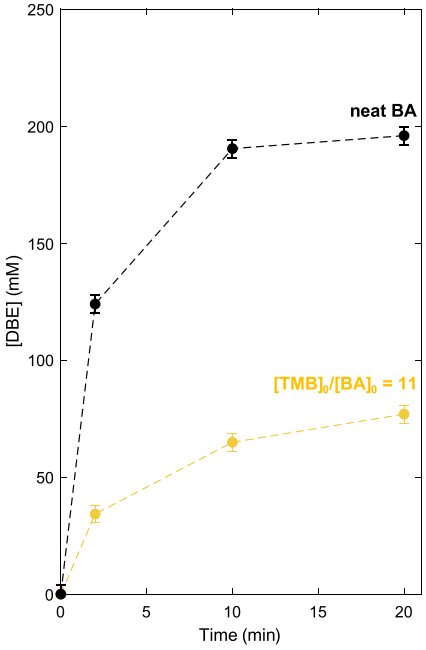

Fig. 9. Temporal [DBE] (mM) (neat BA, 393 K, 0.1 g BEA, 9.8 mL total batch volume). The dashed line is to guide the eye.

coke accumulated in MOR-h (19 ± 1 wt-%) than in MOR (10 ± 1 wt-%) despite equivalent moles of consumed BA (and similar closed mass balances). This outcome was rationalized by the demonstrated ability of mesopores to provide additional access points to protons in micropores that bypass occluded diffusion paths [13,22]. We propose that the mesopores themselves in MOR-h did not contain protons because they

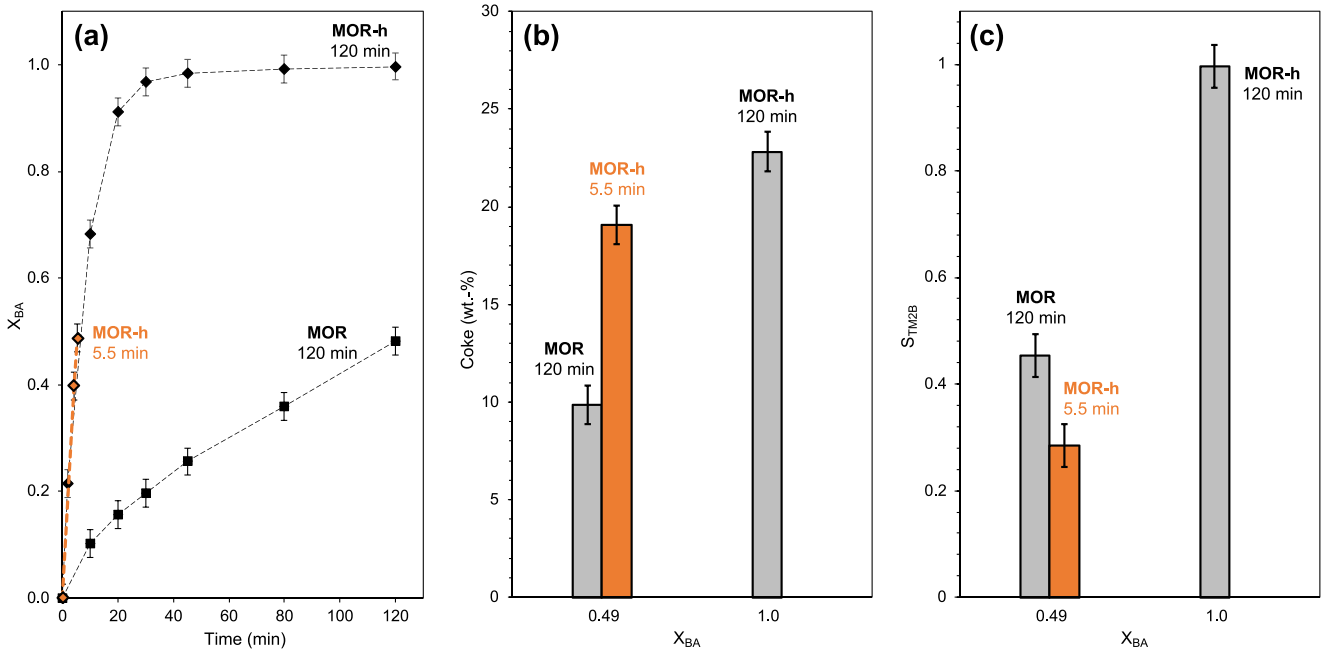

Fig. 10. (a) Temporal X_{BA} for alkylation-etherification (393 K, 0.1 g zeolite, 9.8 mL total batch volume, $[TMB]_0/[BA]_0 = 17$) on MOR-h and MOR, truncated at 120 min (◆, ■) or 5.5 min (♦). Corresponding (b) coke accumulation (wt.-%) and (c) S_{TM2B}.

were introduced through successive dealumination (in HNO_3) and desilication (in NaOH) of MOR to respectively cleave Al-O and Si-O bonds. The resulting dealumination and desilication regimes were exclusively terminated at mesopore surfaces with silanol (Si-OH) groups rather than protons. Previous diffuse reflectance infrared Fourier transform spectroscopy of desilicated MFI indicated that the relative bulk ratio of hydrophilic silanol groups to protons increased with desilication time, consistent with greater water uptake at ambient temperature of more severely desilicated MFI at ambient temperature [22]. Therefore, all the internal protons were expected to be located in the micropores rather than the mesopores of the post-synthetically synthesized MOR-h.

3.5. *Comparing relative production and consumption rates of the intermediate product (DBE) to quantify deviations from kinetically controlled rates due to deactivation*

The observed changes in measured apparent reaction rates after coking compelled investigation of how deactivation impacts secondary reactions in more complex reaction networks. We probed this scenario by considering how coking affected the net consumption rates of DBE, which was shown to undergo a secondary conversion when [BA]/[DBE] > 0.9, which was achieved at $X_{BA} > 0.9$ or could hypothetically be achieved by cofeeding DBE [17]. $[DBE]_{max}$ occurred when DBE consumption and formation rates converge:

$$k_E K_{BA}[BA]^{\beta} = k_{A2} K_{DBE}[DBE]_{max}[TMB] \quad (12a)$$

Again, a reduced order for BA self-etherification from second-order (n = 2) to $\beta = (n + 1)/2 = 1.5$ was used based on the reported correction for the apparent reaction order in the diffusion limit [42]. There was a net consumption of DBE when the following condition is satisfied:

$$k_E K_{BA}[BA]^{1.5} < k_{A2} K_{DBE}[DBE][TMB] \quad (12b)$$

This work sought to understand the potential role of deactivation in triggering this condition. It was unclear if DBE consumption rates exceeded DBE formation rates when coking had somehow rendered the zeolite void environments ineffective for BA self-etherification, or if

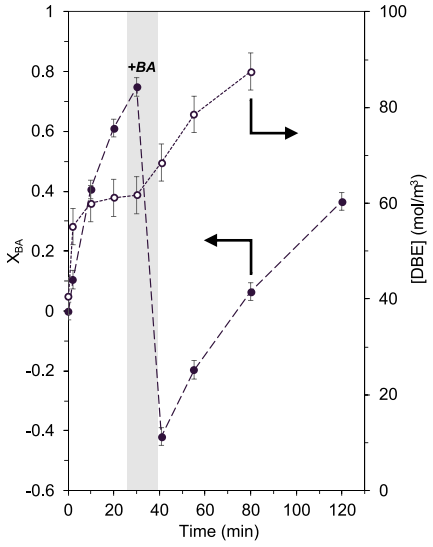

Fig. 11. Temporal X_{BA} (●) and [DBE] (mol/m^3; ○) for TMB alkylation (393 K, $[TMB]_0/[BA]_0 = 33$, 0.1 g BEA, 9.8 mL total batch volume), with BA spiked at 40 min.

concentrations of BA and DBE had decreased and increased, respectively to threshold values that satisfied Eq. (12b). The cause was deduced by spiking additional BA at the $[DBE]_{max}$ observed for $[TMB]_0/[BA]_0 = 33$ (Fig. 11). The spiked BA prevented onset of dominant DBE consumption, indicating that this onset was primarily controlled by relative concentrations of BA and DBE. We therefore concluded that the condition of Eq. (12b) was not met due to prohibition of DBE formation in pores constricted or occluded by coke.

The value of X_{BA} when convergence occurred (Eq. (12a) was thus primarily governed by [BA]/[DBE]. However, it remained possible that coking also caused the convergence values of [BA]/[DBE] and X_{BA} to slightly shift if intrinsic reaction rate constants changed in tandem with progressive occlusion of the local confining environment. If coking did not impact intrinsic reaction rate constants, then reactions on the same

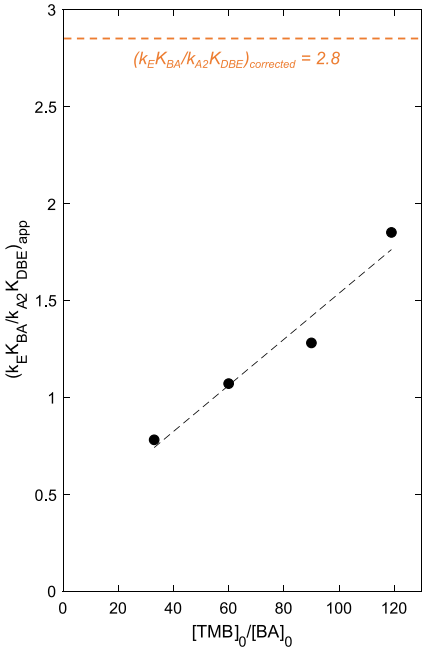

Fig. 12. Calculated values of $(k_EK_{BA}/k_{A2}K_{DBE})_{app}$ as a function of $[TMB]_0/[BA]_0$ for $[TMB]_0/[BA]_0$ = 33, 60, 90, 119.

catalyst (i.e., BEA) for different $[TMB]_0/[BA]_0$ would reach $[DBE]_{max}$ at equivalent X_{BA}. However, we observed that the X_{BA} at $[DBE]_{max}$ did increase with $[TMB]_0/[BA]_0$. This shift is analyzed by rearranging Eq. (12a):

$$\left(\frac{k_EK_{BA}}{k_{A2}K_{DBE}}\right)_{maxDBE} = \frac{[DBE]_{max}[TMB]}{[BA]^{\beta}} \quad (13a)$$

In molar excess of TMB, $[TMB] \approx [TMB]_0$:

$$\left(\frac{k_EK_{BA}}{k_{A2}K_{DBE}}\right)_{maxDBE} = \frac{[DBE]_{max}[TMB]_0}{[BA]^{\beta}} \quad (13b)$$

Thus, Eq. (13b) gives the ratio of apparent rate constants for DBE formation and consumption at $[DBE]_{max}$. Calculations of $(k_EK_{BA}/k_{A2}K_{DBE})_{maxDBE}$ from experimental [BA], $[DBE]_{max}$, and $[TMB]_0$ for $[TMB]_0/[BA]_0$ = 33, 60, 90, 119 were useful because fitted rate constants were only available for initial data ($t \leq 2$ min), when intrinsic rates were very different because coke accumulation was much lower at early times. $(k_EK_{BA}/k_{A2}K_{DBE})_{maxDBE}$ were compared to a diffusion-corrected analog, $(k_EK_{BA}/k_{A2}K_{DBE})_{corrected}$, which was calculated using Thiele modulus formalisms previously derived to deconvolute mass transport artifacts from measured reaction rate constants [17].

$$(k_EK_{BA})_{corrected} = \frac{\rho_{H+}R^2}{D_{BA}}\left[\frac{k_EK_{BA}}{3}\right]^2 \quad (14)$$

$$(k_{A2}K_{DBE})_{corrected} = \frac{\rho_{H+}R^2}{D_{TMB}}\left[\frac{k_{A2}K_{DBE}}{3}\right]^2 \quad (15)$$

The ratio of Eq. (14) and Eq. (15) gave the expression for $(k_EK_{BA}/k_{A2}K_{DBE})_{corrected}$:

$$\left(\frac{k_EK_{BA}}{k_{A2}K_{DBE}}\right)_{corrected} = \frac{D_{TMB}(k_EK_{BA})^2}{D_{BA}(k_{A2}K_{DBE})^2} \quad (16)$$

Values for D_{TMB} (4.6×10^{-13} cm^2/s) and D_{BA} (2.5×10^{-9} cm^2/s) at 393 K were respectively estimated from reported diffusivities of TMB and ethylbenzene in BEA [17,50,51]. Values for apparent k_EK_{BA} and $k_{A2}K_{DBE}$ for Eqs. (14)–(16) were determined from nonlinear regression of

Table 5
$[TMB]_0/[BA]_0$, BEA mass loadings, $[BA]_0/[H^+]_0$, and $X_{BA,\ 120\ min}$. Values in parenthesis are 95 % confidence intervals.

Symbol	$[TMB]_0/[BA]_0$	mass BEA (g)	$[BA]_0/[H^+]_0$	$X_{BA,\ 120\ min}$
●	17	0.1	55	0.61 (0.03)
●	33	0.05	55	0.63 (0.03)
●	33	0.1	28	0.97 (0.03)

reaction data for $[TMB]_0/[BA]_0 = 119$ at $t \leq 2$ min, when deactivation conditions during reaction were minimal. We found that $(k_EK_{BA}/k_{A2}K_{DBE})_{maxDBE}$ increased with $[TMB]_0/[BA]_0$ to approach the value of $(k_EK_{BA}/k_{A2}K_{DBE})_{corrected} = 2.8$ (Fig. 12). The increase of $(k_EK_{BA}/k_{A2}K_{DBE})_{maxDBE}$ values toward $(k_EK_{BA}/k_{A2}K_{DBE})_{corrected} = 2.8$ was consistent with decreasing coking rates with increasing $[TMB]_0/[BA]_0$. It also agreed with observed decreases in coke accumulation with increasing $[TMB]_0/[BA]_0$. A positive slope (Fig. 12) indicates that the DBE formation rate (i.e., the numerator of Eq. (13)) is more severely damped by coke accumulation than the DBE consumption rate. This greater impact of coking on intrinsic DBE formation rates initially seems counterintuitive because DBE consumption involves bulkier reaction moieties (TMB and DBE) than DBE formation (which only involves BA). However, the relative sizes of the transition states must also be considered. It remains unclear whether DBE consumption involves a concerted reaction with TMB or whether it involves a rapid intermediate reaction that is not detectable by ^1H NMR of the reaction liquid. Alternatively, coke may alter the proton distribution whereby different proton locations selectively catalyze DBE formation or consumption. Either way, the magnitude of the unitless slope quantifies this relative damping, with the current value below unity (slope = + 0.012) indicating that the DBE formation rate is impacted by coking 100 times more severely than the DBE consumption rate.

The linearity of the approach to $(k_EK_{BA}/k_{A2}K_{DBE})_{corrected} = 2.8$ indicates the relative damping remains constant across all $[TMB]_0/[BA]_0$ explored in this work; this linearity is expected to persist beyond our studied range of $[TMB]_0/[BA]_0$ = 11–119 because the DBE formation and consumption occur within the same pores ofBEA. Linearity is only expected to deviate in cases where DBE consumption and formation occur exclusively in vastly different confining environments (i.e., small micropores versus the external crystal surface) that are uniquely impacted by accumulating coke. Such a scenario may occur in MFI, where formation of TM2B from DBE consumption with TMB is expected to exclusively occur at the crystal surface, and where DBE formation through self-etherification of BA is feasible at internal protons. Regardless of the (non)linear approach to $(k_EK_{BA}/k_{A2}K_{DBE})_{corrected} = 2.8$, the value of $[TMB]_0/[BA]_0$ at which $(k_EK_{BA}/k_{A2}K_{DBE})_{maxDBE} = (k_EK_{BA}/k_{A2}K_{DBE})_{corrected}$ hypothetically corresponds to the maximum initial concentration of BA at which coking will allow for intrinsic kinetics.

The deactivation arguments deduced from this paper assumed that any catalyst that achieved $X_{BA} = 1$ did so in the limit of $[BA]/[H^+] \gg 1$. Otherwise, if $[BA]/[H^+] \ll 1$ was true, then the excess of protons would mean that measured reaction rates were unaffected by coking. Indeed, all $[TMB]_0/[BA]_0$ here satisfied $[BA]_0/[H^+]_0 \gg 1$. Any temporal changes in [BA] and $[H^+]$ due to respective reaction and deactivation were not expected to cause excursions from $[BA]/[H^+] \gg 1$.

To validate our assumption that $[BA]/[H^+] \gg 1$, we varied $[BA]_0/[H^+]_0$ for different $[TMB]_0/[BA]_0$ by changing mass loadings of BEA (Table 5). For $[TMB]_0/[BA]_0 = 33$, total product concentrations ([DBE] + [TM2B]) overlapped as functions of X_{BA} (Fig. 13a) even when $[BA]_0/[H^+]_0$ differed by a factor of two ($[BA]_0/[H^+]_0$ = 28 and 55). This was only possible if $[BA]/[H^+] \gg 1$ remained true throughout both reactions, such that both reactions operated in the limit of $[TMB]_0/[BA]_0 = 33$. These overlapping profiles were also consistent with minimal product consumption during coking, which again was likely seeded by

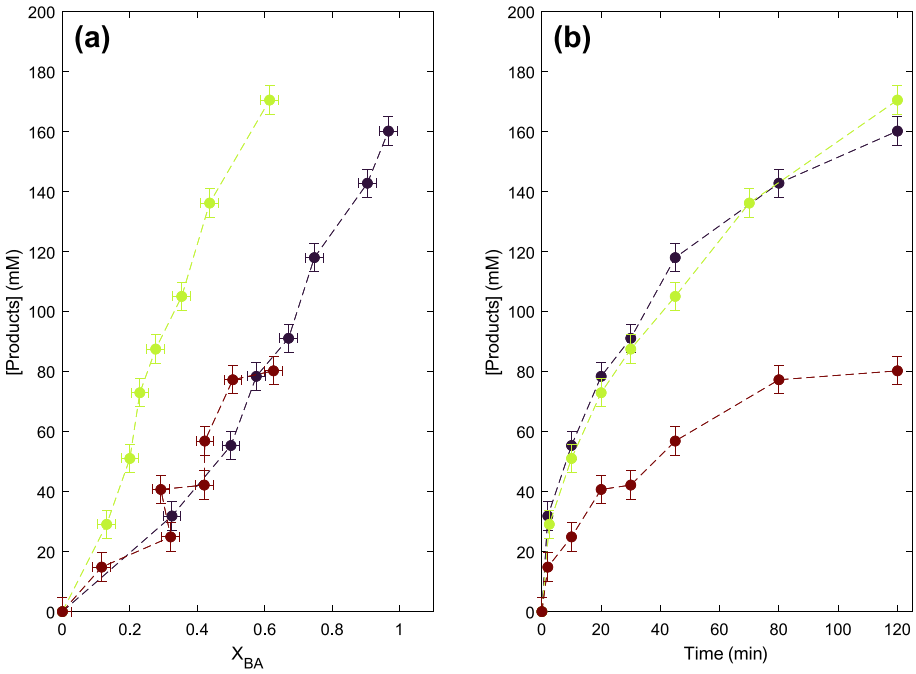

Fig. 13. (a) Total product concentrations (mM) as a function of X_{BA} and (b) as a function of reaction time for $[TMB]_0/[BA]_0 = 33$ [0.05 g BEA (maroon) and 0.1 g BEA (black)] or $[TMB]_0/[BA]_0 = 17$ and 0.1 g BEA (green). All reactions were performed at 393 K with a 9.8 mL batch volume.

very small quantities of (oxygenated) product that did not affect product mass balances. In contrast, temporal product concentrations (functions of time rather than of X_{BA}) overlapped for equivalent catalyst mass loadings (0.1 g BEA) when $[TMB]_0/[BA]_0$ and $[BA]_0/[H^+]_0$ both differed (Fig. 13b). This overlap of temporal product concentrations is only made possible by the condition that $[BA]/[H^+] \gg 1$. In the presence of deactivation, higher product formation rates on $[TMB]_0/[BA]_0 = 17$ than $[TMB]_0/[BA]_0 = 33$ were tempered by concomitantly higher coking rates for $[TMB]_0/[BA]_0 = 17$, causing their net product formation rates to converge. If $[BA]/[H^+] \ll 1$, then no rate changes would manifest from deactivation due to the excess of active sites. Therefore, the differences in $[TMB]_0/[BA]_0$ effectively probed deactivation because $[BA]/[H^+] \gg 1$ was satisfied.

4. Conclusions

This work demonstrated that reaction and deactivation kinetics in (hierarchical) zeolites were closely intertwined in systems involving (poly)substituted aromatic molecules that rapidly underwent coking. The susceptibility of (hierarchical) zeolites to the kinetic consequences of coking depended on nuanced textural and chemical properties (i.e., mesoporosity, parent architecture, crystal size, proton density, silanol density), which we controlled by independently changing deactivation rates as a function of $[TMB]_0/[BA]_0$ on a single zeolite (BEA) for the alkylation-etherification probe network at the nexus of this work.

For a constant reaction time of 120 min, foulant accumulations decreased and X_{BA} increased with $[TMB]_0/[BA]_0$. Between the two foulant classes (low organics and graphitic coke), a significantly higher slope extracted from linear regression of coke accumulation (wt.-%) as a function of $\ln([TMB]_0/[BA]_0)$ indicated that coke caused measurable damping of alkylation and etherification rates, whereas low organics did not. We concluded that coke formation was largely propagated by TMB solvent molecules that underwent polyalkylation, which was seeded by DBE in quantities too small to prevent observably closed BA mass balances for $[TMB]_0/[BA]_0 = 11$–119. This coke manifested in measurable deactivation rate constants ($k_{D,0}$) extracted from a second-order decay law fit to initial concentration data. These $k_{D,0}$ scaled logarithmically with $[TMB]_0/[BA]_0$. Separable reaction-deactivation kinetics enabled extraction of apparent rate constants, which we inferred changed as the confining environments around zeolitic protons were progressively occluded by coking. Values of apparent rate constants approached those of their intrinsic counterparts as $[TMB]_0/[BA]_0$ increased, demonstrating that the accumulations (and hence, impacts) of coke decreased when fewer oxygenated coking seeds were present. Hierarchical zeolites delayed the onset of kinetically relevant deactivation, despite accumulating more coke than their microporous parents at equivalent X_{BA}. These kinetics insights provided necessary intuition and contextualization for deactivation in (hierarchical) zeolites, and more generally, in solid porous catalysts for diffusion-constrained reaction systems.

CRediT authorship contribution statement

Hayat I. Adawi: Writing – review & editing, Writing – original draft, Visualization, Investigation, Formal analysis, Data curation. **Michele L. Sarazen:** Writing – review & editing, Project administration, Methodology, Investigation, Funding acquisition, Conceptualization.

Declaration of competing interest

The authors declare that they have no known competing financial interests or personal relationships that could have appeared to influence the work reported in this paper.

Data availability

Data will be made available on request.

Acknowledgements

The authors acknowledge support High Meadows Environmental Institute Grand Challenge Award at Princeton University, the National Science Foundation (NSF-EFRI CBET-2029425), and the use of the Princeton University NMR Facility. The authors also acknowledge the use of Princeton's Imaging and Analysis Center, which is partially supported through the Princeton Materials Institute (PMI), a National Science Foundation (NSF)-MRSEC program (DMR-2011750). Finally, the

authors acknowledge Jun Zhi Tan and Cole Hullfish for scientific discussions.

Appendix A. Supplementary material

Supplementary data to this article can be found online at https://doi.org/10.1016/j.jcat.2024.115456.

References

[1] R. Gounder, A.J. Jones, R.T. Carr, E. Iglesia, Solvation and acid strength effects on catalysis by faujasite zeolites, J. Catal. 286 (2012) 214–223, https://doi.org/10.1016/j.jcat.2011.11.002.

[2] R. Gounder, E. Iglesia, Catalytic consequences of spatial constraints and acid site location for monomolecular alkane activation on zeolites, J. Am. Chem. Soc. 131 (2009) 1958–1971, https://doi.org/10.1021/ja808292c.

[3] R. Gounder, E. Iglesia, The catalytic diversity of zeolites: confinement and solvation effects within voids of molecular dimensions, Chem. Commun. 49 (2013) 3491–3509, https://doi.org/10.1039/c3cc40731d.

[4] M.L. Sarazen, E. Doskocil, E. Iglesia, Effects of void environment and acid strength on alkene Oligomerization selectivity, ACS Catal. 6 (2016) 7059–7070, https://doi.org/10.1021/acscatal.6b02128.

[5] M.L. Sarazen, E. Iglesia, Effects of Charge, size, and shape of transition states, bound intermediates, and confining voids in reactions of alkenes on solid acids, ChemCatChem 10 (2018) 4028–4037, https://doi.org/10.1002/cctc.201800401.

[6] M.L. Sarazen, E. Doskocil, E. Iglesia, Catalysis on solid acids: mechanism and catalyst descriptors in oligomerization reactions of light alkenes, J. Catal. 344 (2016) 553–569, https://doi.org/10.1016/j.jcat.2016.10.010.

[7] C.H. Bartholomew, Mechanisms of catalyst deactivation, Appl. Catal. A Gen. 212 (2001) 17–60.

[8] M. Guisnet, P. Magnoux, Coking and deactivation of zeolites. influence of the pore structure, Appl. Catal. 54 (1989) 1–27, https://doi.org/10.1016/S0166-9834(00)82350-7.

[9] R.G. Grim, A.T. To, C.A. Farberow, J.E. Hensley, D.A. Ruddy, J.A. Schaidle, Growing the bioeconomy through catalysis: a review of recent advancements in the production of fuels and chemicals from syngas-derived oxygenates, ACS Catal. 9 (2019) 4145–4172, https://doi.org/10.1021/acscatal.8b03945.

[10] M. Guisnet, "Coke" molecules trapped in the micropores of zeolites as active species in hydrocarbon transformations, J. Mol. Catal. A Chem. 182–183 (2002) 367–382, https://doi.org/10.1016/S1381-1169(01)00511-8.

[11] M. Guisnet, L. Costa, F.R. Ribeiro, Prevention of zeolite deactivation by coking, J. Mol. Catal. A Chem. 305 (2009) 69–83, https://doi.org/10.1016/j.molcata.2008.11.012.

[12] K. Lee, S. Lee, Y. Jun, M. Choi, Cooperative effects of zeolite mesoporosity and defect sites on the amount and location of coke formation and its consequence in deactivation, J. Catal. 347 (2017) 222–230, https://doi.org/10.1016/j.jcat.2017.01.018.

[13] M. Milina, S. Mitchell, P. Crivelli, D. Cooke, J. Pérez-Ramírez, Mesopore quality determines the lifetime of hierarchically structured zeolite catalysts, Nat. Commun. 5 (2014), https://doi.org/10.1038/ncomms4922.

[14] P. Iadrat, N. Horii, T. Atithep, C. Wattanakit, Effect of pore connectivity of pore-opened hierarchical MOR zeolites on catalytic behaviors and coke formation in ethanol dehydration, ACS Appl. Mater. Interfaces. 13 (2021) 8294–8305, https://doi.org/10.1021/acsami.0c19780.

[15] L. Gueudré, M. Milina, S. Mitchell, J. Pérez-Ramírez, Superior mass transfer properties of technical zeolite bodies with hierarchical porosity, Adv. Funct. Mater. 24 (2014) 209–219, https://doi.org/10.1002/adfm.201203557.

[16] P. Peng, X.H. Gao, Z.F. Yan, S. Mintova, Diffusion and catalyst efficiency in hierarchical zeolite catalysts, Natl. Sci. Rev. 7 (2020) 1726–1742, https://doi.org/10.1093/nsr/nwaa184.

[17] H.I. Adawi, F.O. Odigie, M.L. Sarazen, Alkylation of poly-substituted aromatics to probe effects of mesopores in hierarchical zeolites with differing frameworks and crystal sizes, Mol. Syst. Des. Eng. 6 (2021) 903–917, https://doi.org/10.1039/d1me00062d.

[18] J. Kim, M. Choi, R. Ryoo, Effect of mesoporosity against the deactivation of MFI zeolite catalyst during the methanol-to-hydrocarbon conversion process, J. Catal. 269 (2010) 219–228, https://doi.org/10.1016/j.jcat.2009.11.009.

[19] H.Y. Luo, J.D. Lewis, Y. Román-Leshkov, Lewis acid zeolites for biomass conversion: perspectives and challenges on reactivity, synthesis, and stability, Annu. Rev. Chem. Biomol. Eng. 7 (2016) 663–692, https://doi.org/10.1146/annurev-chembioeng-080615-034551.

[20] J.Q. Bond, A.A. Upadhye, H. Olcay, G.A. Tompsett, J. Jae, R. Xing, D.M. Alonso, D. Wang, T. Zhang, R. Kumar, A. Foster, S.M. Sen, C.T. Maravelias, R. Malina, S.R. H. Barrett, R. Lobo, C.E. Wyman, J.A. Dumesic, G.W. Huber, Production of renewable jet fuel range alkanes and commodity chemicals from integrated catalytic processing of biomass, Energy Environ. Sci. 7 (2014) 1500–1523, https://doi.org/10.1039/c3ee43846e.

[21] D. Liu, X. Zhang, A. Bhan, M. Tsapatsis, Activity and selectivity differences of external brønsted acid sites of single-unit-cell thick and conventional MFI and MWW zeolites, Microporous Mesoporous Mater. 200 (2014) 287–290, https://doi.org/10.1016/j.micromeso.2014.06.029.

[22] H.I. Adawi, Y. Zheng, M.L. Sarazen, Underpinnings of Carbonaceous deposition among structurally diverse Hierarchical zeolites during Hydrocarbon upgrading, Cryst. Growth Des. 23 (2023) 2675–2688, https://doi.org/10.1021/acs.cgd.2c01488.

[23] H.S. Fogler, Catalyst Decay, in: Elem. Chem. React. Eng., Wiley, 2006.

[24] N. Chaouati, A. Soualah, M. Chater, M. Tarighi, L. Pinard, Mechanisms of coke growth on mordenite zeolite, J. Catal. 344 (2016) 354–364, https://doi.org/10.1016/j.jcat.2016.10.011.

[25] A.T. Aguayo, A.G. Gayubo, A. Atutxa, M. Olazar, J. Bilbao, Catalyst deactivation by coke in the transformation of aqueous ethanol into hydrocarbons. kinetic modeling and acidity deterioration of the catalyst, Ind. Eng. Chem. Res. 41 (2002) 4216–4224, https://doi.org/10.1021/ie020068i.

[26] H.C. Beirnaert, J.R. Alleman, G.B. Marin, A fundamental kinetic model for the catalytic cracking of alkanes on a USY zeolite in the presence of coke formation, Ind. Eng. Chem. Res. 40 (2001) 1337–1347, https://doi.org/10.1021/ie000497l.

[27] I. Hita, H.O. Mohamed, Y. Attada, N. Zambrano, W. Zhang, A. Ramírez, P. Castaño, Direct analysis at temporal and molecular level of deactivating coke species formed on zeolite catalysts with diverse pore topologies, Catal. Sci. Technol. 13 (2023) 1288–1300, https://doi.org/10.1039/d2cy01850k.

[28] N. Taufiqurrahmi, A.R. Mohamed, S. Bhatia, Deactivation and coke combustion studies of nanocrystalline zeolite beta in catalytic cracking of used palm oil, Chem. Eng. J. 163 (2010) 413–421, https://doi.org/10.1016/j.cej.2010.07.049.

[29] P. Pérez-Uriarte, A. Ateka, A.G. Gayubo, T. Cordero-Lanzac, A.T. Aguayo, J. Bilbao, Deactivation kinetics for the conversion of dimethyl ether to olefins over a HZSM-5 zeolite catalyst, Chem. Eng. J. 311 (2017) 367–377, https://doi.org/10.1016/j.cej.2016.11.104.

[30] S. Wan, C. Waters, A. Stevens, A. Gumidyala, R. Jentoft, L. Lobban, D. Resasco, R. Mallinson, S. Crossley, Decoupling HZSM-5 catalyst activity from deactivation during upgrading of pyrolysis oil vapors, ChemSusChem 8 (2015) 552–559, https://doi.org/10.1002/cssc.201402861.

[31] C.D. Prater, R.M. Lago, The Kinetics of the Cracking of Cumene by Silica-Alumina Catalysts, in: W.G. Frankenburg, V.I. Komarewsky, E.K.B.T.-A. in C. Rideal (Eds.), Academic Press, 1956: pp. 293–339. https://doi.org/https://doi.org/10.1016/S0360-0564(08)60543-X.

[32] A.J. Voorhies, Carbon formation in catalytic Cracking, Ind. Eng. Chem. 37 (1945) 318–322, https://doi.org/10.1021/ie50424a010.

[33] S. Lee, M. Choi, Unveiling coke formation mechanism in MFI zeolites during methanol-to-hydrocarbons conversion, J. Catal. 375 (2019) 183–192, https://doi.org/10.1016/j.jcat.2019.05.030.

[34] B.L. Foley, B.A. Johnson, A. Bhan, A method for assessing catalyst deactivation: a case study on methanol-to-Hydrocarbons conversion, ACS Catal. 9 (2019) 7065–7072, https://doi.org/10.1021/acscatal.9b01106.

[35] C.W. Hullfish, J.Z. Tan, H.I. Adawi, M.L. Sarazen, Toward intrinsic catalytic rates and selectivities of zeolites in the presence of limiting diffusion and deactivation, ACS Catal. 13 (2023) 13140–13150, https://doi.org/10.1021/acscatal.3c03559.

[36] R. Giudici, H.W. Kouwenhoven, R. Prins, Comparison of nitric and oxalic acid in the dealumination of mordenite, Appl. Catal. A Gen. 203 (2000) 101–110, https://doi.org/10.1016/S0926-860X(00)00470-1.

[37] X.F. Li, R. Prins, J.A. van Bokhoven, Synthesis and characterization of mesoporous mordenite, J. Catal. 262 (2009) 257–265, https://doi.org/10.1016/j.jcat.2009.01.001.

[38] J.C. Groen, T. Sano, J.A. Moulijn, J. Pérez-Ramírez, Alkaline-mediated mesoporous mordenite zeolites for acid-catalyzed conversions, J. Catal. 251 (2007) 21–27, https://doi.org/10.1016/j.jcat.2007.07.020.

[39] J.W.M. Osterrieth, J. Rampersad, D. Madden, N. Rampal, L. Skoric, B. Connolly, M. D. Allendorf, V. Stavila, J.L. Snider, R. Ameloot, J. Marreiros, C. Ania, D. Azevedo, E. Vilarrasa-Garcia, B.F. Santos, X.H. Bu, Z. Chang, H. Bunzen, N.R. Champness, S. L. Griffin, B. Chen, R.B. Lin, B. Coasne, S. Cohen, J.C. Moreton, Y.J. Colón, L. Chen, R. Clowes, F.X. Coudert, Y. Cui, B. Hou, D.M. D'Alessandro, P.W. Doheny, M. Dincă, C. Sun, C. Doonan, M.T. Huxley, J.D. Evans, P. Falcaro, R. Ricco, O. Farha, K.B. Idrees, T. Islamoglu, P. Feng, H. Yang, R.S. Forgan, D. Bara, S. Furukawa, E. Sanchez, J. Gascon, S. Telalović, S.K. Ghosh, S. Mukherjee, M. R. Hill, M.M. Sadiq, P. Horcajada, P. Salcedo-Abraira, K. Kaneko, R. Kukobat, J. Kenvin, S. Keskin, S. Kitagawa, K. Ichi Otake, R.P. Lively, S.J.A. DeWitt, P. Llewellyn, B.V. Lotsch, S.T. Emmerling, A.M. Pütz, C. Martí-Gastaldo, N. M. Padial, J. García-Martínez, N. Linares, D. Maspoch, J.A. Suárez del Pino, P. Moghadam, R. Oktavian, R.E. Morris, P.S. Wheatley, J. Navarro, C. Petit, D. Danaci, M.J. Rosseinsky, A.P. Katsoulidis, M. Schröder, X. Han, S. Yang, C. Serre, G. Mouchaham, D.S. Sholl, R. Thyagarajan, D. Siderius, R.Q. Snurr, R. B. Goncalves, S. Telfer, S.J. Lee, V.P. Ting, J.L. Rowlandson, T. Uemura, T. Iiyuka, M.A. van der Veen, D. Rega, V. Van Speybroeck, S.M.J. Rogge, A. Lamaire, K. S. Walton, L.W. Bingel, S. Wuttke, J. Andreo, O. Yaghi, B. Zhang, C.T. Yavuz, T. S. Nguyen, F. Zamora, C. Montoro, H. Zhou, A. Kirchon, D. Fairen-Jimenez, How reproducible are Surface areas calculated from the BET equation? Adv. Mater. 34 (2022) https://doi.org/10.1002/adma.202201502.

[40] J.C. Groen, L.A.A. Peffer, J. Pérez-Ramírez, Pore size determination in modified micro- and mesoporous materials pitfalls and limitations in gas adsorption data analysis, Microporous Mesoporous Mater. 60 (2003) 1–17, https://doi.org/10.1016/S1387-1811(03)00339-1.

[41] M. Thommes, K. Kaneko, A.V. Neimark, J.P. Olivier, F. Rodriguez-Reinoso, J. Rouquerol, K.S.W. Sing, Physisorption of gases, with special reference to the evaluation of surface area and pore size distribution (IUPAC technical report), Pure Appl. Chem. 87 (2015) 1051–1069, https://doi.org/10.1515/pac-2014-1117.

[42] M.E. Davis, R.E. Davis, Fundamentals of chemical reaction engineering, McGraw-Hill, 2003.

[43] K. Zhang, S. Fernandez, J.T. O'Brien, T. Pilyugina, S. Kobaslija, M.L. Ostraat, Organotemplate-free synthesis of hierarchical beta zeolites, Catal. Today. 316 (2018) 26–30, https://doi.org/10.1016/j.cattod.2017.11.033.

[44] X. Zhang, D. Liu, D. Xu, S. Asahina, K.A. Cychosz, K.V. Agrawal, Y. Al Wahedi, A. Bhan, S. Al Hashimi, O. Terasaki, M. Thommes, M. Tsapatsis, M. Thommes, M. Tsapatsis, Synthesis of Self-Pillared Zeolite Nanosheets by Repetitive Branching, Sci. 80 (336) (2012) 1684–1687.

[45] D. Xu, O. Abdelrahman, S.H. Ahn, Y. Guefrachi, A. Kuznetsov, L. Ren, S. Hwang, M. Khaleel, S. Al Hassan, D. Liu, S.B. Hong, P. Dauenhauer, M. Tsapatsis, A quantitative study of the structure–activity relationship in hierarchical zeolites using liquid-phase reactions, AIChE J. 65 (2019) 1067–1075, https://doi.org/10.1002/aic.16503.

[46] F.L. Bleken, K. Barbera, F. Bonino, U. Olsbye, K.P. Lillerud, S. Bordiga, P. Beato, T. V.W. Janssens, S. Svelle, Catalyst deactivation by coke formation in microporous and desilicated zeolite H-ZSM-5 during the conversion of methanol to hydrocarbons, J. Catal. 307 (2013) 62–73, https://doi.org/10.1016/j.jcat.2013.07.004.

[47] Y.P. Khitev, I.I. Ivanova, Y.G. Kolyagin, O.A. Ponomareva, Skeletal isomerization of 1-butene over micro/mesoporous materials based on FER zeolite, Appl. Catal. A Gen. 441–442 (2012) 124–135, https://doi.org/10.1016/j.apcata.2012.07.010.

[48] N.M. Tukur, S. Al-Khattaf, Catalytic transformation of 1,3,5-trimethylbenzene over a USY zeolite catalyst, Energy Fuel 21 (2007) 2499–2508, https://doi.org/10.1021/ef7002602.

[49] H. Schulz, “Coking” of zeolites during methanol conversion: basic reactions of the MTO-, MTP- and MTG processes, Catal. Today. 154 (2010) 183–194, https://doi.org/10.1016/j.cattod.2010.05.012.

[50] J. Čejka, J. Kotrla, A. Krejčí, Disproportionation of trimethyl benzenes over large pore zeolites: catalytic and adsorption study, Appl. Catal. A Gen. 277 (2004) 191–199, https://doi.org/10.1016/j.apcata.2004.09.012.

[51] R. Roque-Malherbe, R. Wendelbo, A. Mifsud, A. Corma, Diffusion of aromatic hydrocarbons in H-ZSM-5, H-beta, and H-MCM-22 zeolites, J. Phys. Chem. 99 (1995) 14064–14071, https://doi.org/10.1021/j100038a043.